Volume 1 | Number 1 | Jan 2013 | Pages 1–100

Nanoscale

www.rsc.org/nanoscale

ROYAL SOCIETY
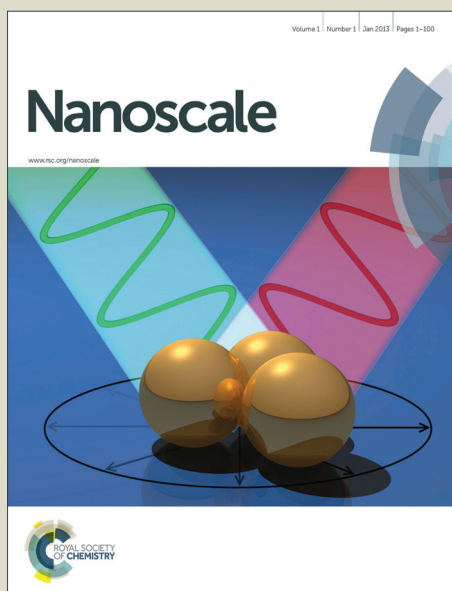OF CHEMISTRY

This is an *Accepted Manuscript*, which has been through the Royal Society of Chemistry peer review process and has been accepted for publication.

Accepted Manuscripts are published online shortly after acceptance, before technical editing, formatting and proof reading. Using this free service, authors can make their results available to the community, in citable form, before we publish the edited article. We will replace this *Accepted Manuscript* with the edited and formatted *Advance Article* as soon as it is available.

You can find more information about *Accepted Manuscripts* in the **Information for Authors**.

Please note that technical editing may introduce minor changes to the text and/or graphics, which may alter content. The journal's standard **Terms & Conditions** and the **Ethical guidelines** still apply. In no event shall the Royal Society of Chemistry be held responsible for any errors or omissions in this *Accepted Manuscript* or any consequences arising from the use of any information it contains.

ARTICLE TYPE

www.rsc.org/xxxxxx | XXXXXXX

MoS$_2$ ultrathin nanosheets obtained under high magnetic field for lithium storage with stable and high capacity

Lin Hu,[a#] Xuyong Feng,[b#] Lingzhi Wei,[a] Kejun Zhang,[c] Jianming Dai,[c] Yucheng Wu,*[b] and Qianwang Chen*[a,d]

5

   A new strategy, namely high magnetic field-induced method,
10 **has been designed to enhance lithium storage properties of**
MoS$_2$ ultrathin nanosheets. The MoS$_2$ ultrathin nanosheets
obtained under 8T exhibit improved cycling stability at the
high current, better rate performance and reduced
electrochemical impedance, compared to those of MoS$_2$
15 **ultrathin nanosheets obtained without the high magnetic field.**
Low-cost, high-energy-density, long-lasting rechargeable
batteries are in high demand to address pressing environmental
needs for energy storage systems that can be coupled to
renewable sources. Lithium-ion batteries (LIBs), owing to their
20 high energy density, light weight, and long cycle life, have shown
considerable promise for use as storage devices.[1-3] Moreover, the
development of electric vehicles and hybrid electric vehicles
demands high power energy sources which can operate under
much higher current condition than the operating current of
25 mobilephones. Also, it is worth mentioning that the
charge/discharge at high currents can shorten the time for practice
applications. However, the charge/discharge process at a high
current rate can cause a high level of polarization for electrode
materials and degrade the electrochemical properties of the
30 batteries. Therefore, many attempts have been made to obtain
qualified electrode materials with high rate performance in past
years.[4-5] Among various electrode materials candidates, layered
transition metal sulfides have gained considerable interest
because of their high theoretical capacities and unique layered
35 structures.[6-8] Molybdenum disulfide (MoS$_2$), as a typical layered
transition metal sulfide with a similar structure to graphite, can
deliver a higher capacity (670 mAh g^{-1} with 4-electron transfer
reaction per formula) than the commercial graphite material (372
mAh g^{-1}).[9-18] Unfortunately, MoS$_2$ exhibits poor intrinsic
40 conductivity due to its large bandgap. Moreover, apart from the
poor intrinsic conductivity, the low conductivity is prone to
appear in nanostructured MoS$_2$ due to the poor interparticle or
interdomain charge transport, which significantly limits the
overall performance. On the other hand, the conversion reaction
45 of MoS$_2$ during Li$^+$ uptake accompanied with the formation of
metal Mo and Li$_2$S. Owing to the low conductivity and poor
cyclability of Li$_2$S, the capacity of MoS$_2$ often fades quickly upon
cycling, especially at high current rates. To date, many research
groups have devoted their attention at enhancing the
50 electrochemical performance and high rate property of MoS$_2$
anodes by using nanotechnologies. In general, structure

modification and combining with other materials (such as
graphene, carbon nanotube, carbon nanofibers) are effective
means to alleviate these problems.[19-33] For example, the most
55 popular approach to increase the capacity is to enlarge the
interlayer distance to relax the strain and lower the barrier for Li
intercalation.[11-13] MoS$_2$ nanoarchitectures anchored into graphene
foam have exhibited enhanced lithium-ion storage. Due to
synergistic effect of the two-component anode, carbon nanofibers
60 decorated with MoS$_2$ nanosheets undergo unprecedented
electrochemical behavior.[21]

   With the development of synthesis and assembly methods,
magnetic field, similar to conventional reaction conditions, such
as temperature, pressure, and surfactant, has been developed as a
65 new parameter for synthesizing and assembling special
nanostructures.[34] To date, there are many examples of
nanomaterials with particular morphologies and enhanced
properties have been achieved in diverse chemical systems (gas,
solution and solid phase) under magnetic fields ranging from
70 several Tesla down to lower than 1T, such as carbon (10T),[35]
TiO$_2$ (9.4T)[36] and Bi (8T).[37] During the synthesis process, when a
high field is employed, the magnetic energy and magnetic force
produced by magnetic fields will become remarkable. As a result,
morphology, domain, crystal structure, product phase and so on,
75 will be significantly influenced. For example, it has been
demonstrated that magnetic field-induced (0.2T) formation of
Fe$_3$O$_4$/C composite microrods exhibited enhanced lithium storage
capability.[38] Recently, Xie et al synthesized MoS$_2$ ultrathin
nanosheets with the expanded interlayer distance and defect-rich
80 structure, and demonstrated the modulations of active sites and
conductivity of MoS$_2$ for hydrogen evolution reaction by increase
the synthesis temperature.[39] Considering the enlarged interlayer
distance and defect-rich structure are beneficial to the increase of
lithium storage capacity,[11-13] we investigated the lithium storage
85 properties of these MoS$_2$ ultrathin nanosheets by using the
standard MoS$_2$/Li half-cell configuration. As expected, capacities
of up to 1200 mAh g^{-1} are attained with high stability at a current
density of 0.1C (1C=1000 mA g^{-1}). However, the capacity fades
quickly when test at 0.5C, which is attributed to poor
90 conductivity because of rich defects and disordering nature in the
product. In other words, although the defects can provide more
active sites to enhance capacity, the low conductivity is also
resulted in due to defect-rich structure, leading to poor cycle
performance at high currents. As discussed above, magnetic field

Nanoscale Accepted Manuscript

is an effective parameter to regulate the nanostructure synthesis. Moreover, it was demonstrated the magnetic field can enhance the conductivity of carbon nanotubes film.[40] Based on these concepts, for the first time, here, the high magnetic field (8T) was employed to control the synthesis of MoS_2 ultrathin nanosheets. It is expected the high magnetic field will improve the conductivity by adjusting the structural parameters of MoS_2 ultrathin nanosheets, and then enhance the lithium storage properties at high currents. For convenience, the resulting MoS_2 ultrathin nanosheets were labeled as B and O, with B indicating the product obtained under a magnetic field of 8T, while O indicating the case without, respectively. It was found that B indeed displayed improved crystallinity and fewer defects compared to those of O, which may be attributed to magnetic field-induced enhanced diffusion of ions and oriented crystal growth during synthesis process. Most importantly, when used as anodes for LIBs, the as-prepared B demonstrated a reversible capacity of 829 mAh g^{-1} after 50 cycles at 0.5C, significantly higher than that of the O. Moreover, the B manifested high cycling stability, better rate behavior and reduced impedance, compared to those of O.

MoS_2 ultrathin nanosheets have been reported in the literature.[39] In the present case, as shown from Fig.1a and 1b, both the O and B display the morphology of nanosheets. Moreover, several big and thick nanosheets can be seen in Fig.1b, as shown by the arrows. From the TEM images (Fig.1c and 1d), graphene-like morphology of O and B can be observed. The obvious ripples and corrugations reveal the ultrathin nature of the nanosheets. The XRD patterns of the O and B are shown in Fig.1g. Both the O and B show two new peaks at the low-angle region. Two additional peaks at $2\theta = 9.32°$ and $18.6°$ are clearly observed in the pattern of O. Using the Bragge-quation, their lattice spacings (d) are estimated to be 9.49 Å and 4.77 Å, respectively. The pattern of B shows two new peaks at $2\theta = 9.06°$ and $18.48°$ with the d of 9.76 Å and 4.8 Å. The diploid relation between the d spacings clearly indicates the formation of a new lamellar structure with enlarged interlayer spacing compared with that of 6.15 Å in pristine 2H-MoS_2 (JCPDS Card No. 73-1508), which is similar to previous results.[39] It is worth mentioning that the B exhibits a little larger d spacings than that of O. Moreover, two broadened peaks at high-angle region can be well indexed to (100) and (110) planes of the pristine 2H-MoS_2. It is noteworthy that the widths of the new peaks in B are narrowed, suggesting the improved crystallinity.[39] Based on above analysis, it is concluded that the B shows larger d spacings and enhanced crystallinity, compared to those of O. The surface electronic state and composition of the product were investigated by XPS analysis. The XPS survey spectrum indicates that both the O and B contain Molybdenum and Sulfur, as shown in Fig.2a. Detailed compositional analysis results reveal that the atomic ratio of Mo : S in O and B are 1: 1.82 and 1: 1.92, which gives the evidence that the as-prepared MoS_2 ultrathin nanosheets possess sulphur vacancy defects. Furthermore, the ICP-AES results are also in close agreement with the above results, which shows the atomic ratio of Mo : S in O and B are 1: 1.83 and 1: 1.94, respectively. It should be noted that the number of sulphur vacancy defects is dependent on the synthesis condition.

Obviously, the O shows more sulphur vacancy defects compared with that in B. Two characteristic peaks arising from Mo $3d_{5/2}$ and Mo $3d_{3/2}$ orbitals are located at 229.1 and 232.1 eV, confirming the dominance of Mo(IV) in the product (Fig.2c). Whereas the binding energies of $S2p_{3/2}$ and $S2p_{1/2}$ are 161.8 eV and 163 eV, respectively, revealing the -2 oxidation chemical state of S (Fig.2b). Furthermore, for the O, the Raman spectrum (Fig. 2d) displays characteristic peaks arising from the E^1_{2g} and A_{1g}. No obvious peak of E_{1g} can be observed. By contrast, for the B, two additional peaks appear. The peak at 283 cm^{-1} attributed to the E_{1g} of 2H-MoS_2, while the 335 cm^{-1} suggests the existence of a considerable amount of 1T phase ingredient embedded in the 2H-MoS_2 host.[41] This result indicates high magnetic field-induced phase transformation occurred during the synthesis process. Moreover, for B, the E^1_{2g} peak is downshifted while the peak of A_{1g} is upshifted, which indicates that the B shows thicker than O sample.[42] Atomic force microscopy (AFM) is also used for assessing the thicknesses of samples (Fig.3). Both O and B have various thicknesses. The most nanosheets possess the thickness under 10 nm. Full nitrogen sorption isotherms were measured to obtain information about the specific surface area and pore sizes of the samples (Fig.S2). The BET surface areas of O and B are 27 and 29 m^2g^{-1}, respectively. The pore size distribution of the as-prepared sample can be gained from the supplied results by using the sorption apparatus. The results demonstrate that both the O and B possess two kinds of pore size.
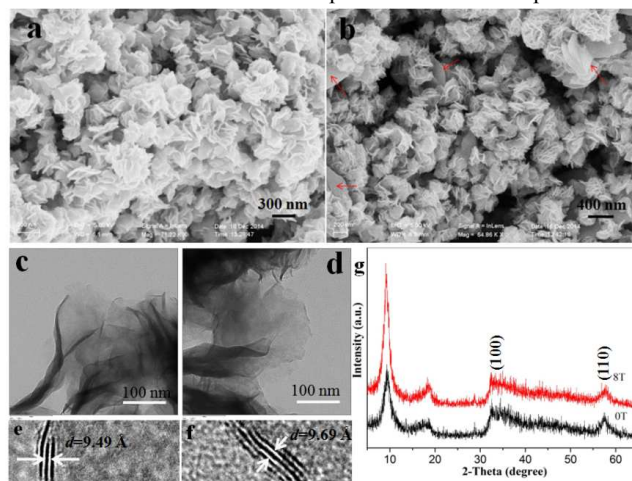
Fig.1 The SEM images of O (a) and B (b); the TEM images of O (c) and B (d); the HRTEM images of O (e) and B (f); (g) the XRD patterns of O and B.
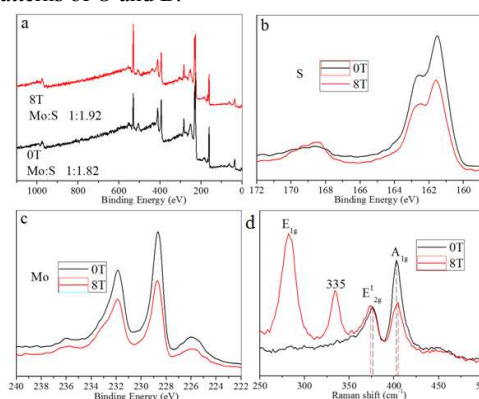
Fig.2 Characterization of the MoS2 nanosheets. XPS spectra of MoS_2 ultrathin nanosheets: (a) survey spectrum; (b) S spectrum; (c) Mo spectrum. (d) Raman spectrum.
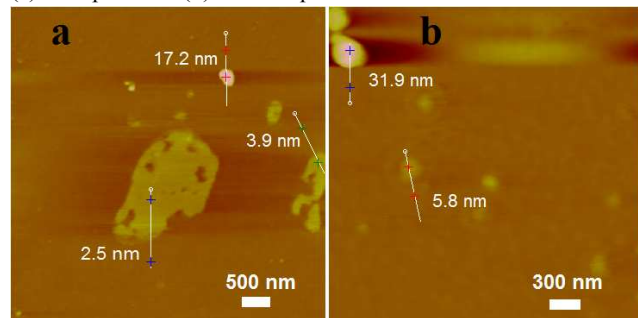
Fig.3 (a) AFM image of O. (b) AFM image of B.

As we known, the high magnetic field, as a special form of extreme conditions, can transfer high energy to the atomic scale of substance, and then change the atomic and molecular arrangement, matching and migration. Therefore, in general, when high magnetic fields are employed during the synthesis process, the behavior of growth units changes (such as atoms, ions, nanocrystallites), and then the final structure get influenced, which is attributed to the reduction in surface energy, orientated growth, and enhancement of the dipole-dipole interaction.[34] In our previous study, it has been proved that the weak magnetic field would induce a convection of the water due to an existed gradient of magnetic susceptibility, which enhances the diffusion of paramagnetic gases (oxygen). As a result, the density of oxygen defects in the product decreased.[43] In the present case, without the magnetic field, the thiourea can be adsorbed on the surface of Mo atom, S atom and primary nanocrystallites, which hinders migration of the growth units, leading to the formation of a defect-rich structure due to confined crystal growth.[44] However, the growth environment is changed when a magnetic field of 8T applies, and it is believed that the high magnetic field can effectively enhance the diffusion of paramagnetic ions to form primary nanocrystallites with fewer defects at the early stage of reaction. After that, the nanocrystallites will grow along the preferential orientation relative to the high magnetic field, leading to the better nanocrystallites orientation (lower degree of disorder), which can be confirmed by the improved crystallinity.[39] Scheme. 1 simply illustrates the formation of the product with and without the high magnetic field.
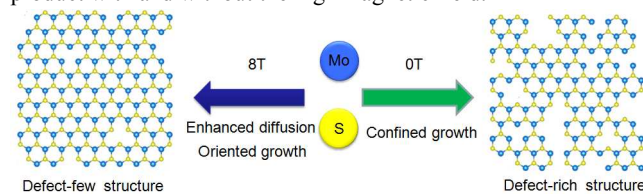

Scheme. 1 Illustration of the formation of MoS_2 ultrathin nanosheets with and without the high magnetic field.

Fig. 4 shows the first three cyclic voltammogram (CV) curves of the electrodes made from O and B. In general, when MoS_2 electrode is cycled between 3.0 and 0.01 V as an anode material, two step reactions occur. First, lithium intercalates into the S slab, and the van der Waals S-S bonds must be broken to be replaced by Li-S bonds. MoS_2 then decomposes into Mo nanoparticles embedded in a Li_2S matrix, corresponding to two cathodic peaks in the first cathodic segment in the cyclic CVs. However, both the O and B only show one obvious peak at 0.33V and 0.36V during the first discharge, respectively. No peaks are observed to 0.9 V during the first discharge. This phenomenon indicates simple topotactic lithium insertion into pristine 2H-MoS_2 phase without phase transition.[11,13] During the first charge processes, both the O and B show two peaks at about 1.75V and 2.25V, which relate to the conversion reaction of Mo and Li_2S to MoS_2 phase. In the following discharge process, the O exhibits a new peak at 1.75V, while a new peak at 1.25V is observed in B. It has been proposed that such peaks formation occurs due to lithium intercalation on different defect sites of MoS_2 developed during the cycling.[11] It should be noted that, for O, the currents at charge processes decrease and the peak positions change with cycling. However, for B, both the currents and peak positions undergo little change, indicating higher stability during cycling and a much better cycling performance can be obtained. Fig. 5a and 5b show the voltage profiles of the O and B during the first and second cycles at a 0.1C rate. For O, the first discharge and charge capacities are 1567 and 1152 mAh g^{-1}, respectively, corresponding to the Coulombic efficiency (CE) of 73.5%. For B, the first discharge and charge capacities are 1167 and 864 mAh g^{-1}, respectively, corresponding to the CE of 74%. After the first cycles, the CE quickly stabilizes at approximately 98%. It is noteworthy that the capacity of both two samples is higher than the theoretical capacity (670 mAh g^{-1} for the reaction: $MoS_2 + 4 Li = 2Li_2S + Mo$), the extra capacity should come from some side reactions like the reaction between Li and electrolyte or lithium storage in active sites. The cycling performance of O and B are tested at the currents of 0.1C and 0.5C, respectively. As shown in Fig. 5c and 5d. The O manifests higher specific capacity (1200 mAh g^{-1}) than that of B (900 mAh g^{-1}) at the current of 0.1C, which is attributed to more active sites and side reactions in O electrode because of the defect-rich structure. After cycling 50 cycles at 0.1C, the capacity of O decreases slightly, while the capacity of B undergoes no changes. However, when tests at the current of 0.5C, the capacity of O fades dramatically, while the B still shows good capacity retention. The discharge capacity of B after 50 cycles is as high as 829 mAh g^{-1} at the current of 0.5C. We believe such performance of B is very attractive among the reported results for MoS_2 electrode. For instance, a restacked MoS_2 electrode exhibited a reversible specific capacity of 750 mAh g^{-1} at the current of 50 mA g^{-1} after 50 cycles.[12] Hierarchical MoS_2 microboxes showed a high capacity of 900 mAh g^{-1} at the current of 100 mA g^{-1} after 50 cycles.[10] MoS_2 nanoflowers demonstrated a discharge capacity of 814 mAh g^{-1} at 100 mA g^{-1} after 50 cycles.[45]

Actually, besides the aspect of active sites, the conductivity of electrode material is another crucial factor to determine the lithium storage property because a high conductivity ensures a fast electron and lithium ion transport during the charge/discharge process. Although defect-rich structure in O will provide abundant active sites to increase the storage capacity, unfortunately, the conductivity in such nanostructured materials is hindered due to the poor interparticle or interdomain

electron/ion transport. Therefore, the O only can exhibit high and stable capacity at the low current (0.1C). When cycled at the high current (0.5C), the electron/lithium ion transport will need to become fast. However, the low conductivity will hamper
5 electron/ion transport, leading to poor cycling performance of O at the high current. During the synthesis process of B, on the one hand the enhanced diffusion of paramagnetic ions and oriented growth will produce fewer defects in nanocrystallites, and on the other high magnetic field-induced phase transformation occurred.
10 The fewer defects and existence of 1T phase can account for the enhanced electrical conductivity. The fewer defects can enhance the interdomain conductivity.[39] 1T phase of MoS_2 is metallic polymorph, which also benefits to enhance conductivity.[46] Moreover, the larger d spacing in B will benefit the Li^+ diffusion,
15 which may be responsible for the increase of ionic conductivity. As a result, the B displays higher and more stable lithium storage property than that of O at 0.5C. Obviously, by means of high magnetic field-induced method, the structure and conductivity MoS_2 ultrathin nanosheets can be regulated at a moderate degree,
20 which is more suitable for lithium storage property at the high current.
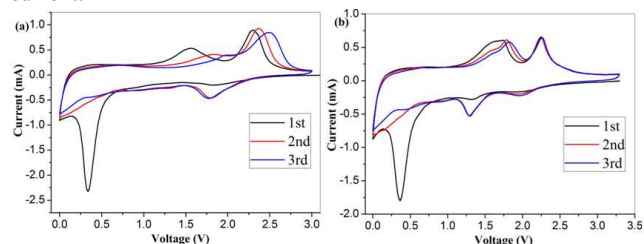
Fig.4 The cyclic voltammograms curves of (a) O and (b) B from 0 V to 3.0 V at the rate of 0.2mV/s.
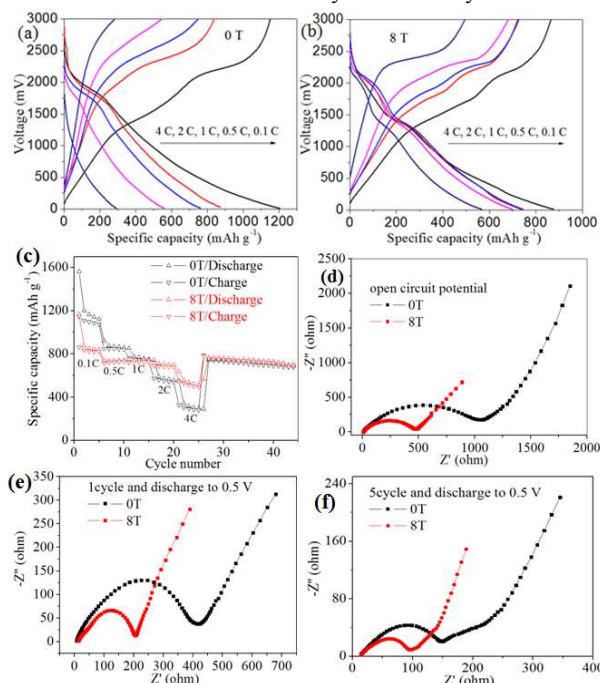
25
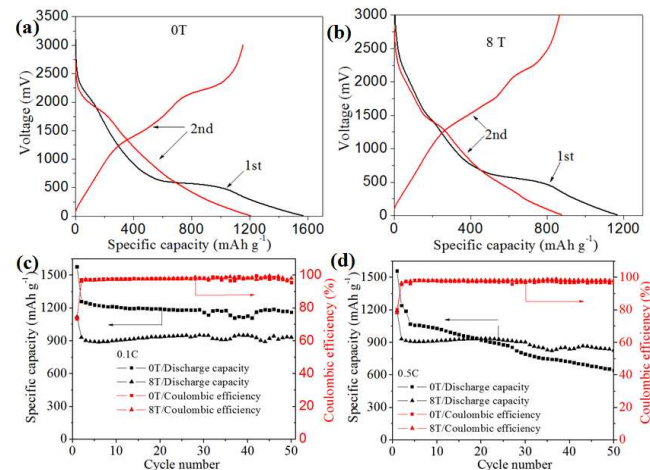
Fig.5 Discharge-charge voltage profiles of (a) O and (b) B. (c) Cycling performance of O and B at a current density of 0.1C.(d) Cycling performance of O and B at a current density of 0.5C.
30 In order to evaluate the rate capability, the O and B electrodes were cycled at various current densities (0.1C-4C) and the charge/discharge curves are shown in Fig. 6a, 6b. Upon gradually elevating the current density, the capacities of O and B fade. The O exhibits higher capacity at low current density (0.1C), but the
35 capacity dramatically decreases at high current densities. Whereas the capacity of B displays slight reduction when

increase the current densities. Indeed, the B exhibits much better rate performance (Fig.6c), especially at the current densities from 0.5C to 2C, compared to that of O. The capacities of O electrode
40 at the currents of 0.1C, 0.5C, 1C, 2C and 4C are 1205, 874, 765, 555 and 288 mAh g^{-1}, respectively. In contrast, the B electrode delivers capacities of 875, 745, 726, 700 and 570 mAh g^{-1}, at the above mentioned current rates, demonstrating an excellent high rate performance for high power lithium ion battery. Moreover, it
45 can clearly see that the capacity of B is higher than that of O at 2C-4C. These results further prove that the B exhibits better lithium storage property at high currents.
In order to further reveal the transport kinetics for the electrochemical properties of the samples, alternating current
50 impedance (AC) measurements were carried out after different cycles. The measured cell is charged to 3 V, and then placed for a period of time to reach a stable state for impedance measurement. The plots consist of a depressed semicircle in the high and middle frequency regions and a straight line in the low-frequency region.
55 The semicircle at high frequency can be assigned to the charge-transfer impedance on electrode-electrolyte interface (Rct). Fig.6 d, 6e and 6f are the impedance spectra of O and B electrodes of fresh cell, after first cycle and fifth cycle, respectively. It is apparent that the semicircle of B is much smaller than that of O,
60 indicating a lower charge transfer resistance compared to O. The Nyquist plots reveal the charge-transfer resistance of O is almost double of that of B. It is worth mentioning that the resistance of electrode is also important for practical application, which is related with the quantity of heat. The small resistance will
65 produce little quantity of heat during the charge/discharge process, which benefits the lifetime and safety of the battery.

Fig.6 (a,b)The galvanostatic discharge-charge voltage profiles of O and B electrodes at different current densities.(c)cycling
70 performance of O and B electrodes at different current densities. (d-f) The impedance spectra of O and B electrodes after different cycles of discharge and recharge at 0.5C.

In summary, for the first time, high magnetic field (8T) was employed to control the synthesis of MoS_2 ultrathin nanosheets. The role of high magnetic field is to enhance the diffusion of paramagnetic ion and induce the oriented growth during the synthesis process, which leads to fewer defects and better nanocrystallites orientation in product that can result in improved conductivity. When test as anodes of LIBs, the product obtained under 0T exhibits a high capacity (1200 mAh g^{-1}) at 0.1C with excellent stability due to the defect-rich structure, but the capacity dramatically fades at 0.5C because of the low conductivity. In contrast, the product obtained under 8T displays high and stable capacity both at 0.1C (900 mAh g^{-1}) and 0.5C (829 mAh g^{-1}), indicating a better performance, especially at the high current. Moreover, the product obtained under 8T demonstrates better rate behavior and smaller resistance, compared to those of the product obtained under 0T. These results prove the high magnetic field can be considered as an effective parameter to adjust the structure of MoS_2 during the synthesis process, and then enhance the lithium storage property. With the appearance of superconducting technology, a high magnetic field which is more than 1T could be obtained easily, which would open a possible way to tailor the structure and property of nanomaterials by applying a high magnetic field.

Notes and references

[a] High Magnetic Field Laboratory, Hefei Institutes of Physical Science, Chinese Academy of Sciences, Hefei, Anhui 230031, P.R. China.

[b] School of Materials Science and Engineering, Hefei University of Technology, Hefei, Anhui 230009, P.R. China.

[c] Institute of Solid State Physics, Hefei Institutes of Physical Science,

[d] Division of Nanomaterials and Chemistry, Hefei National Laboratory for Physical Sciences at the Microscale, Department of Materials Science and Engineering, University of Science and Technology of China, Hefei, Anhui 230026, P.R. China.

# These authors contributed equally to this work.

*Corresponding authors. E-mail addresses: E-mail: cqw@ustc.edu.cn; ycwu@hfut.edu.cn.

† Electronic Supplementary Information (ESI) available: Experimental details, Surface area.
DOI: 10.1039/b000000x/

1 P. Poizot, S. Laruelle, S. Grugeon, L. Dupont and J. M. Tarascon, *Nature*, 2000, **407**, 496.

2 X. L. Ji, K. T. Lee and L.F. Nazar, *Nat. Mater.*, 2009, **8**, 500.

3 B. Scrosati, J. Hassoun and Y. K. Sun, *Energy Environ. Sci.*, 2011, **4**, 3287.

4 B. Kang and G. Ceder, *Nature*, 2009, **458**, 7235.

5 K. Kang, Y. S. Meng, J. Breger, C. P. Grey and G. Ceder, *Science*, 2006, **311**, 977.

6 F. Bonaccorso, L. Colombo, G. H. Yu, M. Stoller, V. Tozzini, A. C. Ferrari, R. S. Ruoff and V. Pellegrini, *Science*, 2015, **347**, 1246501.

7 R. T. Lv, J. A. Robinson, R. E. Schaak, D. Sun, Y. F. Sun, T. E. Mallouk and M.Terrones, *Acc. Chem. Res.*, 2015, **48**, 56.

8 M. Chhowalla, H. S. Shin, G. Eda, L. J. Li, K. P. Loh and H. Zhang, *Nat. Chem.*, 2013, **5**, 263.

9 S. J. Ding, D. Y. Zhang, J. S. Chen and X.W. Lou, *Nanoscale*, 2012, **4**, 95.

10 L. Zhang, H. B. Wu, Y. Yan, X. Wang and X. W. Lou, *Energy Environ. Sci.*, 2014, **7**, 3302.

11 H. Hwang, H. Kim and J. Cho, *Nano Lett.*, 2011, **11**, 4826.

12 G. D. Du, Z. P. Guo, S. Q. Wang, R. Zeng, Z. X. Chen and H. K. Liu, *Chem. Commun.*, 2010, **46**, 1106.

13 H. Liu, D. W. Su, R. F. Zhou, B. Sun, G. X. Wang and S. Z. Qiao, *Adv. Energy Mater.*, 2012, **2**, 970.

14 X. F. Wang, Z. R. X. Guan, Y. Y. Li, Z. X. Wang and L. Q. Chen, *Nanoscale*, 2015, **7**, 637.

15 G. D. Li, X. Y. Zeng, T. D. Zhang, W. Y. Ma, W. P. Li and M. Wang, *CrystEngComm*, 2014, **16**, 10754.

16 D.Y. Chen, G. Ji, B. Ding, Y. Ma, B. H. Qu, W. X. Chen and J. Y. Lee, *Ind. Eng. Chem. Res.*, 2014, **53**, 17901.

17 U. K. Sen and S. Mitra, *ACS Appl. Mater. Interfaces.*, 2013, **5**, 1240.

18 M. Wang, G. D. Li, H. Y. Xu, Y. T. Qian and J. Yang, *ACS Appl. Mater. Interfaces.*, 2013, **5**, 1003.

19 H. J. Yoo, A. P. Tiwari, J. T. Lee, D. Kim, J. H. Park and H. Lee, *Nanoscale*, 2015, **7**, 3404.

20 T. Stephenson, Z. Li, B. Olsen and D. Mitlin, *Energy Environ. Sci.*, 2014, **7**, 209.

21 F. Zhou, S. Xin, H. W. Liang, L. T. Song and S.H. Yu, *Angew. Chem. Int. Ed.*, 2014, **53**, 11552.

22 J. Wang, J. L. Liu, D. L. Chao, J. X. Yan, J. Y. Lin and Z. X. Shen, *Adv. Mater.*, 2014, **26**, 7162.

23 Z. M. Wan, J. Shao, J. J. Yun, H. Y. Zheng, T. Gao, M. Shen, Q. T. Qu and H. H. Zheng, *Small*, 2014, **10**, 4975.

24 X. S. Zhou, L. J. Wan and Y. G. Guo, *Nanoscale*, 2012, **4**, 5868.

25 K. Chang and W. X. Chen, *ACS Nano*, 2011, **6**, 4720.

26 J. Xiao, D. W. Choi, L. Cosimbescu, P. Koech, J. Liu and J. P. Lemmon, *Chem. Mater.*, 2010, **22**, 4522.

27 K. Chang and W. X. Chen, *Chem. Commun*, 2011, **47**, 4252.

28 X. H. Cao, Y. M. Shi, W. H. Shi, X. H. Rui, Q. Y. Yan, J. Kong, H. Zhang, *Small*, 2013, **9**, 3433.

29 L.C. Yang, S. N. Wang, J. J. Mao, J. W. Deng, Q. S. Gao, Y. Tang, O. G. Schmidt, *Adv. Mater.*, 2013, **25**, 1180.

30 K. Bindumadhavan, S. K. Srivastava and S. Mahanty, *Chem. Commun.*, 2013, **49**, 1823.

31 H. L. Yu, C. Ma, B. H. Ge, Y. J. Chen, Z. Xu, C. L. Zhu, C. Y. Li, Q. Y. Ouyang, P. Gao, J. Q. Li, C. W. Sun, L. H. Qi, Y. M. Wang and F. H. Li, *Chem. Eur. J.*, 2013, **19**, 5818.

32 S. K. Park, S. H. Yu, S. Woo, B. Quan, D. C. Lee, M. K. Kim, Y. E. Sung and Y.Z. Piao, *Dalton Trans.*, 2013, **42**, 2399.

33 C. F. Zhang, Z. Y. Wang, Z. P. Guo and X. W. Lou, *ACS Appl. Mater. Interfaces.*, 2012, **4**, 3765.

34 L. Hu, R. R. Zhang and Q. W. Chen, *Nanoscale*, 2014, **6**, 14064.

35 G. P. Vilas, V. P. Swati, A. Gedanken, M. G. Sung and S. Asai, *Carbon*, 2004, **42**, 2735.

36 N. Attan, H. Nur, J. Efendi, H. O. Lintang, S. L. Lee and I. Sumpono, *Chem. Lett.*, 2012, **41**, 1468.

37 Y. B. Xu, Z. M. Ren, W. L. Ren, G. G. Cao, K. Deng and Y. B. Zhong, *Nanotechnology*, 2008, **19**, 115602.

38 Y. R. Wang, L. Zhang, X. H. Gao, L.Y. Mao, Y. Hu and X.W. Lou, *Small*, 2014, **10**, 2815.

39 J. F. Xie, J. J. Zhang, S. Li, F. Grote, X. D. Zhang, H. Zhang, R. X. Wang, Y. Lei, B. C. Pan and Y. Xie, *J. Am. Chem. Soc.*, 2013, **135**, 17881.

40 L. Valentini, M. Cardinali, D. Bagnis and J. M. Kenny,

Carbon, 2008, **46**, 1506.

41 L. Cai, J. F. He, Q. H. Liu, T. Yao, L. Chen, W. S. Yan, F. C. Hu, Y. Jiang, Y. D. Zhao, T. D. Hu, Z. H. Sun and S. Q. Wei, *J. Am. Chem. Soc.*, 2015, **137**, 2622.

42 Y. C. Wang, J. Z. Ou, S. Balendhran, A. F. Chrimes, M. Mortazavi, D. D. Yao, M. R. Field, K. Latham, V. Bansal, J. R. Friend, S. Zhuiykov, N. V. Medhekar, M. S. Strano and K. Kalantar-zadeh, *ACS NANO*, 2013, 7, 10083.

43 Z. M. Peng, J. Wang, Y. J. Huang and Q. W. Chen,

Chem.Eng.Technol., 2004, **24**, 1273.

44 J. F. Xie, H. Zhang, S. Li, R. X. Wang, X. Sun, M. Zhou, J. F. Zhou, X. W. Lou and Y. Xie, *Adv. Mater.*, 2013, **25**, 5807.

45 Y. Y. Lu, X. Y. Yao, J. Y. Yin, G. Peng, P. Cui and X. X. Xu, *RSC Adv.*, 2015, 5, 7938

46 M. A. Lukowski, A. S. Daniel, F. Meng, A. Forticaux, L. S. Li, and S. Jin, *J. Am. Chem. Soc.*, 2013, **135**, 10274.

Nanoscale Accepted Manuscript